



Role of the metal cation in the dehydration of the microporous metal–organic frameworks CPO-27-M

Mali H. Rosnes^a, Breogán Pato-Doldán^{a,1}, Rune E. Johnsen^b, Alexander Mundstock^c, Jürgen Caro^c, Pascal D.C. Dietzel^{a,*}

^a Department of Chemistry, University of Bergen, P.O. Box 7803, 5020, Bergen, Norway

^b Department of Energy Conversion and Storage Technical University of Denmark, Frederiksborgvej 399, DK-4000, Roskilde, Denmark

^c Institute of Physical Chemistry and Electrochemistry, Leibniz University Hannover, Callinstr. 3A, D-30167, Hannover, Germany

ARTICLE INFO

Keywords:

Metal-organic frameworks
CPO-27-M
M-MOF-74
In situ techniques
Thermal analysis
X-ray diffraction
Phase transitions
Dehydration

ABSTRACT

The dehydration of the CPO-27-M (M-MOF-74, M = Zn, Co, Ni, Mg, Mn, Cu) metal-organic framework series has been investigated comprehensively using *in situ* variable temperature powder X-ray diffraction (VT-PXRD) and thermal analysis (TG) coupled with mass spectrometry (MS). Significant differences in the order of water desorption from different adsorption sites on heating are found with varying metal cation in the otherwise isostructural material. For all CPO-27-M (except M = Cu), water is bonded significantly more strongly to the accessible open metal sites, and these water molecules are only desorbed at higher temperatures than the other water molecules. CPO-27-Cu is an exception, where all water molecules desorb simultaneously and at much lower temperatures (below 340 K). MS and TG data show that all CPO-27-M start to release traces of CO₂ already at 300–350 K, and thus long before bulk thermal decomposition is observed. Only for CPO-27-Co, the CO₂ release is essentially constant on its baseline between 450 and 700 K, and it is the only CPO-27-M member that shows a stable plateau in the TG in this region. Additional rehydration studies on CPO-27-Co show that the MOF incorporates any water molecules present until the pores are fully loaded. CPO-27-Co consequently behaves as an efficient trap for any water present.

1. Introduction

Metal-Organic Frameworks (MOFs) are coordination networks composed of metal moieties and organic ligands that (at least potentially) contain voids [1]. Due to their porous nature and exceptionally high surface areas this class of materials is particularly attractive for applications in catalysis, gas storage, separation processes and as potential sensor material [2–13]. It is of paramount importance for their applications to understand how MOFs behave upon dehydration and, in particular, whether they remain stable upon solvent removal [14–17]. In addition, several MOFs are currently investigated for water harvesting applications, and the understanding of the water stability and degradation mechanisms is vital for the development of next generation MOF-based water adsorbents [18–29].

There are different mechanisms for the removal of solvent molecules and avoiding the collapse of the structure [30]. In some cases exceptionally large breathing has been identified [31–36], as well as more

complex single-crystal-to-single-crystal transformations [37–42]. Other frameworks manage the solvent removal by the re-arrangement of the coordination environment of the metal, either by a change in coordination number and/or geometry [43–46], or by the substitution of the former solvent molecule with a less volatile ligand [47]. It has also been found that the dehydration can occur despite the lack of clear transport channels, indicating that cooperative structural exchange and replacement occur for water to leave the structure [48].

In the case of the isostructural series CPO-27-M, also denoted M₂(dhtp), M₂(dobdc) (dhtp/dobdc = 2,5-dioxido-1,4-benzenedicarboxylate C₈H₂O₆⁴⁻) or M-MOF-74, where M = Co [49], Ni [50], Mg [51], Mn [52], Zn [53], Fe [54,55], and Cu [56], the framework is robust enough to accommodate an empty coordination site at the metal after desolvation [49,50,57,58]. The presence of non-occupied coordination sites (open metal sites) renders the materials extremely interesting for applications relying on interaction with guest molecules in the pore [59–70]. The dehydration processes of CPO-27-Co and Zn were

* Corresponding author.

E-mail address: pascal.dietzel@uib.no (P.D.C. Dietzel).

¹ Current address: Insud Farma. Laboratorios León Farma, S.A. C/La Vallina, s/n 24193, Navatejera - León, España.

investigated previously by *in situ* variable temperature powder X-ray diffraction (VT-PXRD), shedding light on the dynamic structural changes occurring upon dehydration and showing distinct differences between the two compounds [58]. CPO-27-Fe has also been investigated previously, and it was found that the iron can actually undergo a change in oxidation state from +2 to +3 and back, corresponding to three different crystalline phases, as methanol from the pore is converted into formaldehyde during the desolvation experiment [54].

Herein, we present the first comprehensive study of the dynamic structural changes in the CPO-27 series upon dehydration, linking VT-PXRD (M = Ni, Mg, Cu and Mn) and TG-MS (M = Ni, Mg, Cu, Mn, Co and Zn) results. The results are also compared with the already available data for CPO-27-Co and -Zn [58]. The combination of VT-PXRD with thermal analysis and the monitoring of the composition of the evolved gas stream through the direct TG-MS coupling gives a unique insight into the dynamic changes these materials undergo during the dehydration process.

The behavior of materials upon hydration is another key aspect for potential applications [71–73]. It has been reported that the gas uptake for CPO-27 deteriorates upon exposure to water vapor, and upon hydration the material has reduced gas uptake capacity [74–84]. CPO-27-Co has been reported to have sensitivity towards humid air [85], causing a surface blockage, completely preventing the adsorption of even small guest molecules. Interestingly, this could at least be partially reversed by contact with methanol. When the desolvated material was exposed to humid atmosphere, a discontinuous phase change was observed by powder X-ray diffraction. This observation was in stark contrast to the continuous phase transition observed during dehydration [58]. Clearly additional investigations of the rehydration behavior of the material are needed, and we therefore performed VT-PXRD experiments to shed more light onto the structural changes observed for CPO-27-Co upon rehydration.

2. Experimental section

All reagents and solvents were purchased from Sigma-Aldrich and used as received without further purification. The samples used for gas adsorption measurements were processed under inert conditions. Gases used for gas adsorption measurements were of 99.9995%, or higher, purity and were purchased from Yara Praxair.

2.1. Instrumentation

2.1.1. Thermal analysis (TG-MS)

Simultaneous thermogravimetry and differential scanning calorimetry with simultaneous monitoring of the evolved gases (TG-DSC-QMS) was performed using a Netzsch Jupiter STA 449 F1 (TGA-DSC), connected to a Netzsch Aëolos QMS 403 C quadrupole mass spectrometer. The temperature program ran from 303 to 873 K, with a heating rate of 2 or 5 K min⁻¹ and an Ar gas flow of 50 mL min⁻¹.

2.1.2. Gas sorption

Nitrogen adsorption was carried out on a BELSORP-max instrument at 77 K to confirm the specific surface area and pore volume for CPO-27-Co used in the rehydration experiment. The sample was prepared under inert conditions and transferred to the sample cell in a glove box. Prior to the measurements, the samples were treated at 423 K for 24 h in a dynamic vacuum.

2.1.3. Variable temperature synchrotron powder X-ray diffraction (VT-PXRD)

Samples were measured at the Swiss–Norwegian Beamlines (BM01) at the European Synchrotron Radiation Facility (ESRF) in Grenoble (France). A specially modified capillary sample holder was used for the variable temperature X-ray powder diffraction experiments [86]. The sample was fixated in a borosilicate glass capillary with the help of a

small amount of glass wool. In a typical experiment, diffraction data was recorded while a slow flow of inert gas (He or Ar) was applied through the capillary and the sample was heated from room temperature with a heating rate of 2 K min⁻¹ below 473 K and of 5 K min⁻¹ above 473 K.

2.1.4. X-ray diffraction of the hydration of CPO-27-Co

A sample of CPO-27-Co was pre-treated in our home lab by heating the sample in a dynamic vacuum until it completely lost the guest water molecules; afterwards it was packed and transported in a sealed capillary. This capillary with the empty MOF was installed in the experimental setup at the beamline. The capillary was opened up and X-ray diffraction data was recorded at 298 K while an Ar stream, which was led through a Woulff's bottle type steel apparatus to saturate it with water vapor, was led through the capillary containing the sample.

2.1.5. X-ray data analysis

Full pattern matching and Rietveld refinements of the powder diffraction patterns were performed using TOPAS 4.2 [87]. Crystal structures of CPO-27-M samples fully loaded with water molecules at room temperature (as-synthesized samples) were solved by simulated annealing and subsequently refined using the Rietveld method. A Chebyshev function of 6 terms was used to fit the background and a broad Pseudo-Voigt peak was used to account for the contribution of the capillary to the background. 14 soft distance restraints and 20 angle restraints were applied to maintain the connectivity of the atoms of the 2, 5-dioxido-1,4-benzenedicarboxylate linker. Anisotropic displacement parameters were defined for all metal atoms, except copper. Isotropic displacement parameters were used for all other atoms in the structure. The resulting crystal structures of the fully hydrated CPO-27-M materials (M = Mg, Mn, Co, Ni, and Zn) were used as starting models for sequential Rietveld refinements [88] performed across the whole temperature range, where the site occupancy factors of the oxygen atoms representing the water molecules were permitted to refine (with a maximum upper limit at 1). The water molecules were allowed to move freely in the whole temperature range. An anti-bump restraint, as implemented in TOPAS, was used to prevent the oxygen atoms of the water molecules from approaching closer than 1.5 Å during the sequential Rietveld refinements. A different approach was implemented with the dehydration experiment of CPO-27-Cu and the hydration experiment of CPO-27-Co, because both samples show a phase mixture at some point of the experiment. In these two cases the starting points of the sequential Rietveld refinements were in the middle of the phase mixture (scan 3959 for CPO-27-Co and 314.8 K for CPO-27-Cu). Two different sequential refinements were then implemented proceeding in both directions of data from the starting point.

2.2. Synthesis

The members of the CPO-27 family with different cations were synthesized according to established procedures: CPO-27-Cu [89], CPO-27-Ni [90], CPO-27-Mg [51], CPO-27-Mn [89], CPO-27-Co [49], CPO-27-Zn [58]. After synthesis, the materials were filtered open to atmosphere and washed with water to replace the solvent from the synthesis with water. All samples were air-dried before being analyzed by TG-MS and VT-PXRD to study the stability of the sample and the behavior upon dehydration.

CPO-27-Co for the hydration experiment was synthesized according to literature procedure [49]. The material was filtered in an inert atmosphere, washed with water and subsequently immersed in methanol for 3 × 30 min to replace all solvent molecules, before being dried at 423 K in dynamic vacuum. The textural properties from the synthesis result in BET specific surface area of 1286 m² g⁻¹, and total pore volume (at $p/p_0 = 0.500$) of 0.48 cm³ g⁻¹.

3. Results and discussion

VT-PXRD experiments were carried out to better understand the behavior of CPO-27-M upon dehydration for M = Ni, Mg, Cu and Mn. The corresponding results for M = Co and Zn have been published previously by us [58]. Complementary information on the behavior upon dehydration was obtained by performing TG-DSC-MS analysis for M = Ni, Mg, Cu, Mn, Co and Zn. We first present the details for each of the members of the series individually before we compare the results and present the investigation of the hydration process for CPO-27-Co.

3.1. Dehydration of CPO-27-Mg

The crystal structure determination of the data collected at room temperature shows that the water molecules occupy five different sites inside the CPO-27-Mg cavities (Fig. 1), in accordance with the previously reported structure [51]. In addition to the water molecule coordinated to the metal cation (O4), there are four crystallographically independent (crystal) water molecules in the structure. Two of these (O5 and O7) have a short O–O distances to O4 (O4...O5 is ~ 2.6 Å, O4...O7 is ~ 3 Å in CPO-27-Mg) that indicates they are hydrogen bonded to the coordinated water. The other two (O6 and O8) have short contacts to O5, O7 and between each other.

VT-PXRD indicates good crystallinity of CPO-27-Mg (Fig. 2a) until 770 K, then decomposition starts. There is no change in the crystalline phase below 823 K, indicating that the dehydration of CPO-27-Mg is a second order process. Only small and smooth changes of reflection positions are observed in the CPO-27-Mg stability range. The most noticeable changes in peak intensity occur between room temperature and 373 K, i.e. in the temperature range where one expects the water to desorb from the pores.

When studying the evolution in occupancy of the water molecules, three different groups can be distinguished (Fig. 2b). The first group corresponds to the water molecules O6 and O8, which mostly leave the framework below 320 K. The second group corresponds to the water molecules O5 and O7, which are hydrogen bonded to the coordinated water (O4) and begin to desorb slightly above 320 K. For both groups, the occupancy of the water molecules is negligible at 350 K. The third group, which consists of the coordinated water molecule (O4), is unaffected until 350 K. Above 350 K the occupancy of this water molecule begins to decrease slowly and smoothly until the dehydration is nearly complete at 460 K.

The observed variation in unit cell parameters is related to the water

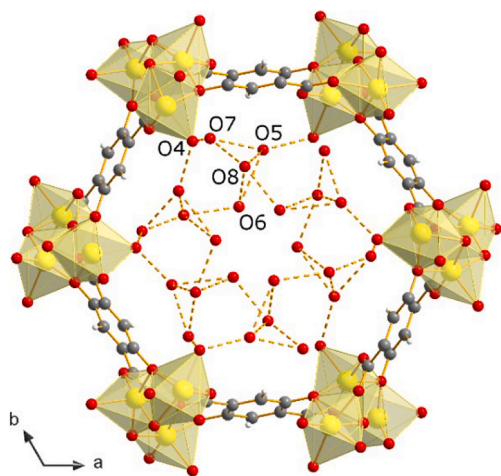


Fig. 1. Excerpt of the crystal structure of CPO-27-Mg, showing one channel with all water molecules present. Short O–O distances below 3 Å are identified by dashed lines. The connectivity is also representative for the other members of the series.

content. Between 293 and 350 K, in accordance with the loss of the non-coordinated water molecules, the *a* parameter decreases, except for a small kink at 323 K. Meanwhile, the *c* axis follows a different tendency; it remains constant between 293 and 323 K and increases between 323 K and 353 K (Fig. 2c). At higher temperatures between 353 and 463 K, the *a* parameter increases and the *c* axis decreases smoothly, in coincidence with the loss of the coordinated water molecule (O4). Finally, above this temperature, when no water molecules are found inside the cavity, the cell parameters remain roughly constant until the final decomposition of the material. There is a significant intensity drop of the peak intensities at 620 K, which indicates the onset of the final decomposition.

When comparing with the previously reported PXRD experiments monitoring the dehydration of CPO-27-Mg [51], we observe that the temperature range where the material appears stable is higher herein, which we ascribe to kinetic effects due to the significantly higher heating rate in this experiment (5 K min^{-1} above 473 K) than in the previous experiments (6 and 16 K h^{-1}).

From the MS traces recorded simultaneously during the TG-DSC measurements of CPO-27-Mg (Fig. 2d), it is apparent that H₂O evolves immediately. The shape of the initial water signal ($m/z = 18$) for CPO-27-Mg is broad with a clear tail from 420 to 650 K. This is also reflected in the TG and DSC traces. There is a fairly stable plateau observed in the TG trace from about 550 to 880 K, with only a minor gradual decline. This coincides with the MS trace for $m/z = 44$ signal (CO₂) that increases (almost imperceptibly) already from 330 K and more noticeably from 500 K. The signal becomes much more intense from 750 K, with a final maximum centered between 850 and 1000 K, which we interpret as evolution of CO₂ from the thermal decomposition of the framework (see Fig. S1). Two independent endothermic peaks are observed in the DSC trace at approx. 800 K and 900–1000 K. Mass loss assigned to the final decomposition of the material commences at 850 K in the TG trace, coinciding with the intense $m/z = 44$ signal between 850 and 1000 K.

3.2. Dehydration of CPO-27-Ni

VT-PXRD shows good crystallinity of CPO-27-Ni (Fig. 3a) in the range of temperatures measured (293–473 K). Only small and smooth changes of reflection positions are observed, mainly in the temperature range between 343 and 373 K. The most noticeable changes in peak intensity occur between room temperature and 373 K. The evolution in occupancy of the water molecules for CPO-27-Ni shows a similar trend to that observed for CPO-27-Mg, where three different groups can be distinguished. The water molecules O6 and O8 leave the framework at temperatures below 340 K and O5 and O7 below 373 K (Fig. 3b). The occupancy of the coordinated water molecule (O4) is stable up to 365 K, at which the occupancy begins to decrease slowly.

The variation in unit cell parameters of CPO-27-Ni (Fig. 3c) show that between 293 and 370 K the *a* parameter decreases, which coincides with the loss of the non-coordinated water molecules. The *a* parameter reverses the trend of its direction and shows a small maximum between 330 and 340 K, then a sharp decrease is observed until 370 K, above which its value declines more slowly. The *c* parameter shows a gentle increase from 293 to 340 K, followed by a much steeper increase from 340 to 375 K. Above 370 K, the *c* parameter decreases in parallel with the *a* parameter, in coincidence with the loss of the coordinated water molecule (O4).

The experimental setup used for this measurement at the synchrotron facility did not allow temperatures above 473 K. An additional set of data covering the full temperature range including the decomposition of the MOF was collected later, and the results from the Rietveld analysis are reported in the SI as an indication of the expected evolution (Figs. S2 and S3). It confirms the trends for the changes in lattice parameter and site occupancy factors discussed above. However, there is an unexpected shift to higher temperatures for these changes. We think this is caused by too much sample packed in the capillary, which means water that is

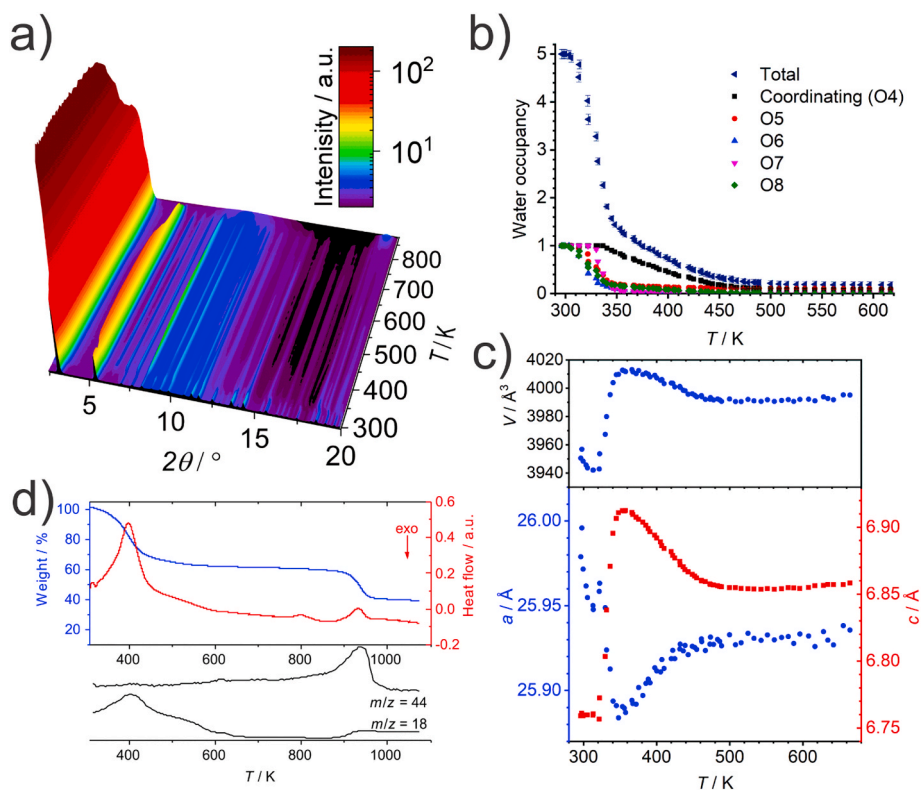


Fig. 2. CPO-27-Mg a) VT-PXRD data in Ar flow. b) Development of the site occupancy factor of the water molecules in the pore as the temperature is increased. c) Temperature dependence of lattice parameters and cell volume. d) Thermal analysis (TG trace: blue, DSC trace: red, MS traces for $m/z = 44$ and 18: black). (For interpretation of the references to color in this figure legend, the reader is referred to the Web version of this article.)

desorbed from the sample material positioned upstream (outside the heating zone) affects the gas phase concentration of water and the equilibrium between adsorption and desorption in the material in the beam. The processes then happen at higher temperature than they would if the inert gas stream was completely dry, e.g. in the MS signal assigned to evolution of the coordinated water molecule remains coordinated until 573 K in this experiment instead of desorbing earlier and at in the MS signal assigned to evolution more realistic lower temperatures.

TG-DSC-MS traces for CPO-27-Ni were recorded in both air and inert atmosphere, with thermal decomposition starting at much lower temperatures in air (around 450 K) than in Ar (about 600 K) (Fig. 2d). For the inert TG-DSC-MS run, H₂O is evolved immediately when the heating program has started (Fig. 3d). The initial MS trace for the $m/z = 18$ signal shows a broad maximum, with a clear shoulder from 420 to 550 K (see Fig. S4 for further details). This coincides with weight loss in the TG trace and an endothermic peak in the DSC trace, as one expects for desolvation. The TG trace shows a semi-stable plateau from 485 to 600 K, with a small gradual decline which is mirrored by a gradual increase in the MS signal assigned to evolution of CO₂ ($m/z = 44$) from about 350 K. This indicates that decomposition of the material might have commenced with a slow rate. Above 550 K the CO₂ trace increases more rapidly, with a local maximum at 620 K before the main maximum at 720 K. This corresponds well with the decomposition of the material, starting just above 600 K according to the TG trace and the corresponding endothermic maximum in the DSC trace, which is in line with previously reported values [50].

3.3. Dehydration of CPO-27-Mn

VT-PXRD attests to the good crystallinity of CPO-27-Mn (Fig. 4a). A sharp change in some reflection positions and intensities is observed between 320 and 340 K, followed by the most significant changes in peak intensities just below 350 K. Afterwards, the intensities remain

fairly unchanged up to about 515 K, followed by a significant decrease between 500 and 550 K. The intensities then decrease more slowly in the range from 550 to 720 K, followed by a second sharp reduction until all reflections belonging to CPO-27-Mn have disappeared and reflections corresponding to manganese oxide appear as result of the final decomposition of the MOF. The observed variation in peak intensities and unit cell parameters is related to the water content (Fig. 4b). Between 293 and 350 K, in coincidence with the loss of the non-coordinated water molecules, the a parameter decreases and the c parameter increases. Between 350 and 390 K, there is a slight decrease in the c parameter, corresponding with the loss of the coordinated water molecule (O4). Above 350 K for the a parameter and above 390 K for the c parameter, the cell parameters remain roughly constant, when almost all of the water molecules have left the pore. At 530 K the values become slightly less stable, especially for the c parameter, where also the FWHM starts to increase, probably because the average crystallite size decreases (Fig. S6). This coincides with the intensity plot for the (110) reflection, suggesting that the structure starts to partly decompose at approx. 520 K, followed by the final decomposition of the sample around 700 K (Fig. S7). Also, the increase in the low-angle scattering intensity at about 530 K shows that small particles or structures with large voids are being formed, which is in agreement with decomposition of the original MOF (Fig. S7).

The **TG-DSC-MS traces** for CPO-27-Mn (Fig. 4d) indicate that H₂O ($m/z = 18$) starts to evolve immediately, corresponding to the solvent loss in the weight signal, and mirrored by a much smaller maximum for CO₂ ($m/z = 44$, Figs. S8 and S9). The shape of the initial MS maximum for $m/z = 18$ for CPO-27-Mn is broad, and only returns back to the base line by 550 K. For $m/z = 44$ the signal returns to the baseline by 475 K. There is an almost stable plateau in the TG and DSC traces from 450 to 770 K. From 495 K there is a gradual increase in the MS trace for the $m/z = 44$ signal, indicating that decomposition of the material has commenced. The $m/z = 44$ signal levels out around 640 K, before an

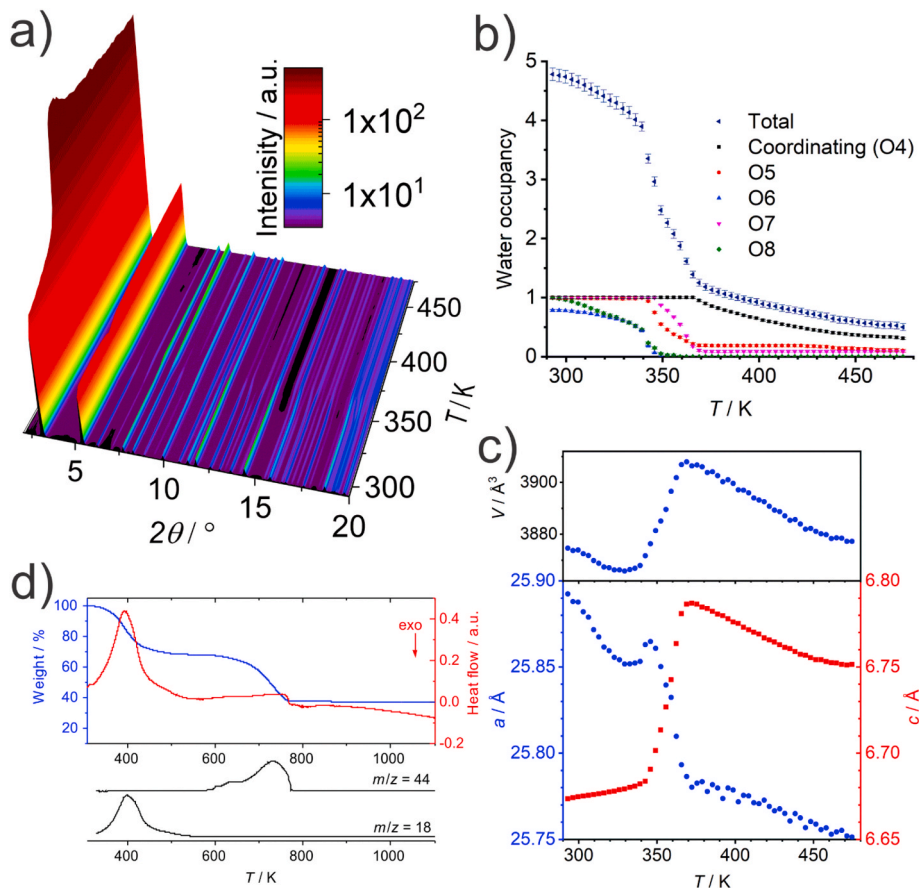


Fig. 3. CPO-27-Ni. a) VT-PXRD data in Ar flow. b) Development of the site occupancy factor of the water molecules in the pore as the temperature is increased. c) Temperature dependence of lattice parameters and cell volume. d) Thermal analysis (TG trace: blue, DSC trace: red, MS traces for $m/z = 44$ and 18: black). (For interpretation of the references to color in this figure legend, the reader is referred to the Web version of this article.)

intense and sharp maximum appears in the range 750–860 K. This is in agreement with the sharp weight loss starting just above 780 K in the TG trace. This limit for the stability of CPO-27-Mn in the TG trace is slightly higher than observed by VT-PXRD.

3.4. Dehydration of CPO-27-Cu

It is well known that CPO-27-Cu shows a different adsorption behavior towards adsorptives such as hydrogen and carbon dioxide than the other members of the CPO-27 series [68,89]. Thus, it is of special interest to investigate how this translates into its behavior during dehydration.

VT-PXRD shows good crystallinity of CPO-27-Cu until it decomposes above 520 K (Fig. S10). A sharp change in some reflection positions and intensities is observed around 313 K (Fig. 5a). Rietveld refinements of the powder diffraction data carried out at temperatures below and above 313 K reveals that there are two phases present that correspond to the hydrated (at 293.15 K, Fig. S11) and dehydrated (at 339.15 K, Fig. S12) forms of CPO-27-Cu. The space groups of the hydrated and dehydrated crystal structures are identical ($R\bar{3}$), with only small differences in the reflection positions and intensities (Fig. 5b and Fig. S13). This makes the quantification of their individual contribution to the overall diffractogram challenging. The Rietveld analyses of the variable temperature diffractograms indicate that the new dehydrated phase first appears around 323 K (Fig. 5c). The two phases coexist in the temperature range 323 K–335 K, with the amount of the dehydrated phase increasing with increasing temperature, until 335 K, where only the dehydrated phase is detected.

Sequential Rietveld refinements reveal the temperature dependence

of the unit cell parameters of the hydrated and dehydrated phases (Fig. 5d). The lattice parameters of the hydrated phase decrease with increasing temperature, with the most pronounced decrease occurring below 298 K. Initially, the cell parameters of the dehydrated phase decrease with increasing temperature, suggesting that the phase still has some residual water in the pores, but quickly the values are relatively constant, indicating that the pores are essentially empty. The a axis parameter differs by about 0.1 Å between the two phases, whilst we observe no significant difference for the c axis parameter. It is evident from the overall water occupancy as a function of temperature that the material transforms from fully hydrated to dehydrated within a temperature range of 30 K (Fig. 5e). The transformation is complete at 335 K. In the water containing phase, which exists below this temperature, two molecules (O6 and O8) start to leave already at 305 K, one just below 313 K (O4, the coordinated water), one at 328 K (O5) and the final one just below 333 K (O7) (Fig. S14). Notably, both water molecules O5 and O7 start to leave the framework after the coordinated water molecule, O4. The process is relatively slow for the first 20 K, before the total water occupancy in the sample is reduced from over 3.5 to zero within the 325–335 K range.

The TG-DSC-MS traces for CPO-27-Cu (Fig. 5f) show that H_2O ($m/z = 18$) evolves immediately from the start of the experiment. From the endothermic peak observed in the DSC trace and the H_2O trace it is evident that the evolution of H_2O is completed abruptly already at 360 K. This is in good agreement with the VT-PXRD data (Fig. 5c and d). Correspondingly, the TG trace shows a plateau from 380 K to 575 K, where only a slight decrease in weight is observed. It coincides with a small increase of signal intensity for $m/z = 30$ and 44 in the MS trace, where $m/z = 44$ is likely CO_2 , indicating either minuscule decomposition

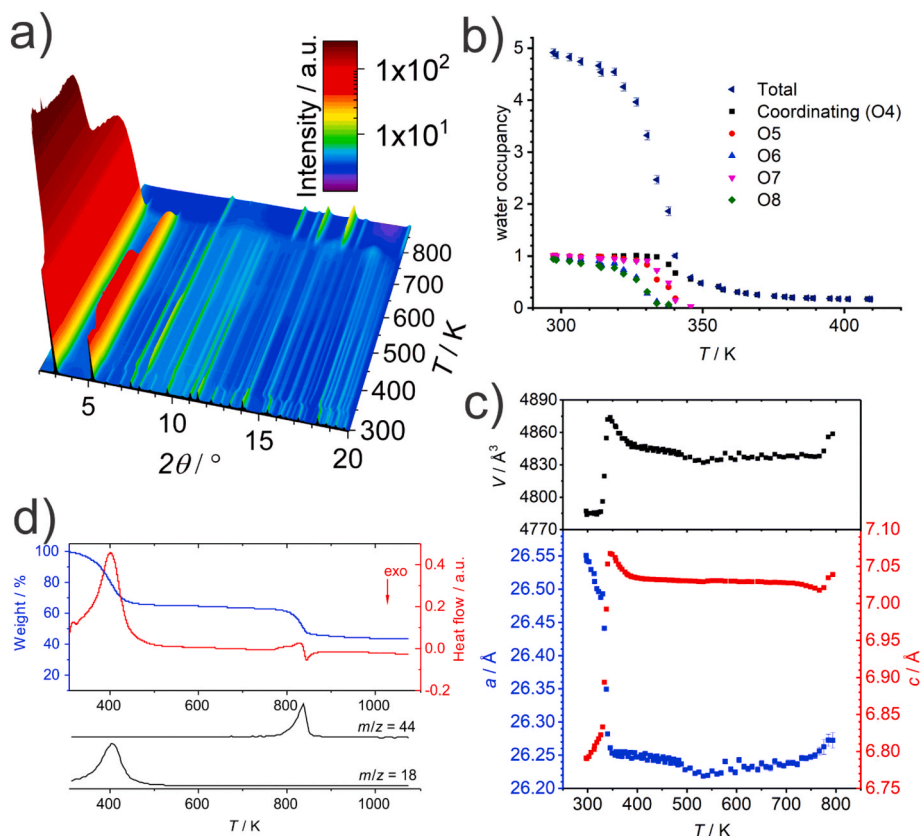


Fig. 4. CPO-27-Mn. a) VT-PXRD data in Ar flow. b) Development of the site occupancy factor of the water molecules in the pore as the temperature is increased. c) Temperature dependence of lattice parameters and cell volume. d) Thermal analysis (TG trace: blue, DSC trace: red, MS traces for $m/z = 44$ and 18 : black). (For interpretation of the references to color in this figure legend, the reader is referred to the Web version of this article.)

of the material or evolution of residual DMF, the solvent used in the synthesis (see Figs. S15 and S16 for further details). Above 550 K the MS trace for $m/z = 44$ increases significantly, as does evolution of oxygen and water, indicating the final decomposition of the framework. This coincides with the sharp weight loss and the endothermic peak just above 600 K. The stability of CPO-27-Cu to about 570 K in the thermal analysis is in good agreement with the VT-PXRD data, where it was found that decomposition occurs above 520 K.

3.5. Dehydration of CPO-27-Co

The TG-DSC-MS traces for CPO-27-Co (Fig. 6) show that the evolution of H_2O ($m/z = 18$) essentially starts as soon as the measurement begins, reaching a maximum at 398 K. The shape of this first MS maximum for $m/z = 18$ is broad, and the signal returns to the baseline only at around 500 K (see Figs. S17 and S18 for further details). This behavior of the water signal is mirrored in the TG and DSC traces that indicate endothermic solvent loss in this temperature range. A stable plateau is observed in the TG trace from 450 to 690 K. There is a maximum of very low intensity for $m/z = 44$ between 320 and 450 K, before the signal remains stable at the base line until 650 K. Just above 675 K a significant shoulder appears prior to the main maximum, observed between 740 and 875 K. Interestingly, these two peaks are clearly present in the DSC trace as two separate endothermic peaks and, to a lesser extent, visible in the sharp decline in the TG between 700 and 800 K. The data show that CPO-27-Co is stable up to 680–690 K and is completely decomposed at around 800 K, which agrees well with the previously reported VT-PXRD data that was recorded using an identical heating program, where it decomposed in the temperature range 723–770 K [58].

3.6. Dehydration of CPO-27-Zn

The TG-DSC-MS traces for CPO-27-Zn (Fig. 7) show that water desorption ($m/z = 18$) starts at low temperatures with a maximum peak at 405 K. The shape of the MS maximum for $m/z = 18$ for CPO-27-Zn is broad, and only returns to the base line by 480 K (see Figs. S19 and S20 for further details). The TG trace has an almost stable plateau between 430 and 500 K, where the gradual decrease can be explained by the slight evolution of water still observed in the MS signal. The MS trace for water has another, weaker peak at 490–590 K, before a smaller second peak at 590–630 K. This coincides with a step in the TG trace, which might be ascribed to the desorption of residual water from the open metal site. However, the water peak ($m/z = 18$) at 590–630 K, the increased CO_2 signal ($m/z = 44$) at 510–660 K, and the small endothermic peak observed in the DSC trace from 500 to 600 K indicate that more is happening here.

There is a gradual decrease observed for the TG signal from 500 K, and due to the lack of a proper plateau it is difficult to identify the onset of decomposition. The MS trace for $m/z = 44$ shows a gradual increase from about 475 K, with the shoulder peak from 510 to 660 K, followed by the main maximum from 660 to 900 K, peaking at 790 K. This indicates that the material starts to decompose slowly already at about 500 K, with onset of final and more rapid decomposition above 730 K. This is in good agreement with previous VT-PXRD data, where it was found that CPO-27-Zn stays basically unchanged until it decomposes in the range 660–760 K [58].

3.7. Comparison of results for the different CPO-27-M materials

VT-PXRD in this and previous studies [50,54,58] show similarities and differences between the different members of the isostructural

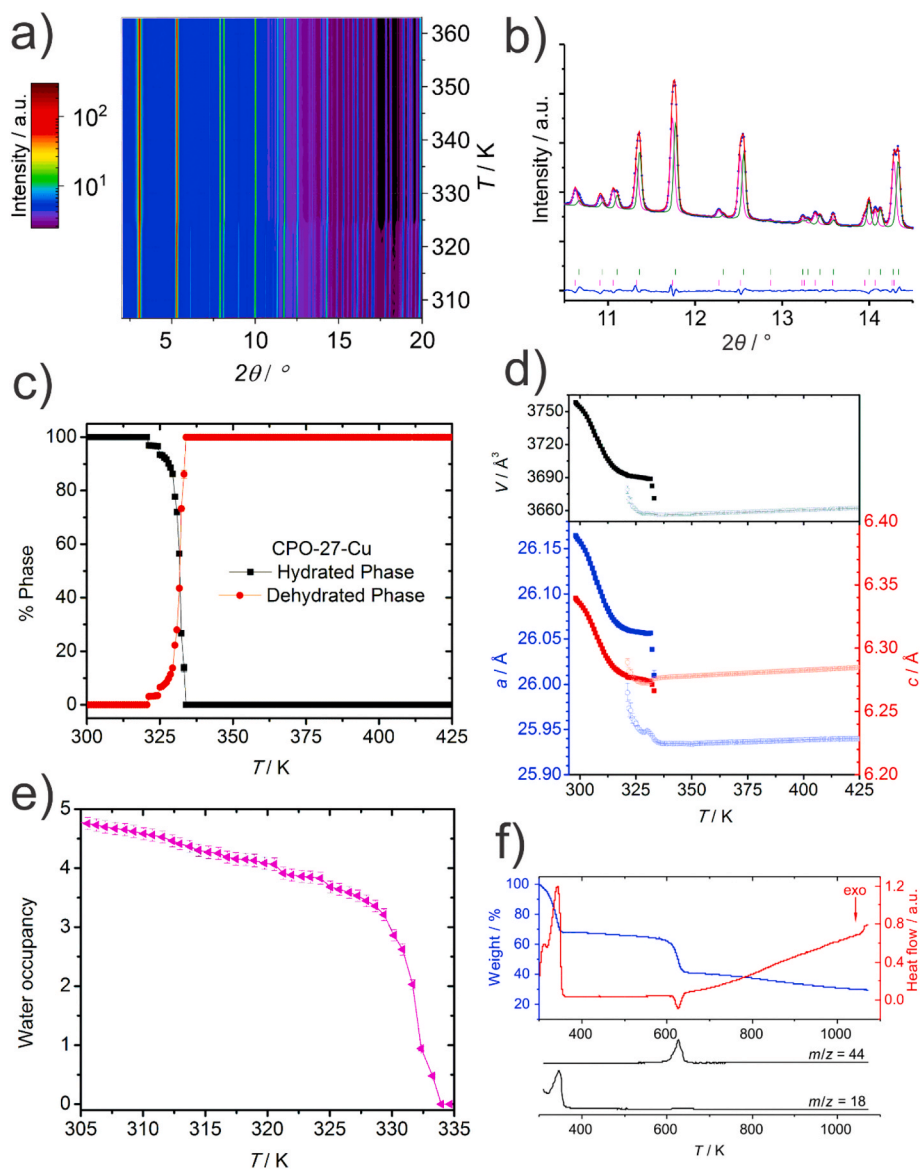


Fig. 5. CPO-27-Cu. a) Intensity profile of the VT-PXRD data of CPO-27-Cu under Ar flow in the temperature range where the hydrated and dehydrated phases coexist. b) Excerpt of the Rietveld refinement plot of data measured at 332 K. The blue points and the red line represent the experimental and calculated diffraction patterns, respectively. The magenta and green lines represent the calculated diffraction patterns for the hydrated and dehydrated forms, respectively. The blue line represents the difference plot. The magenta and green tick marks represent the Bragg reflections for the hydrated and dehydrated forms, respectively. c) Temperature dependence of the phase ratio for hydrated and dehydrated CPO-27-Cu. d) Temperature dependence of the unit cell parameters for the hydrated and dehydrated phase of CPO-27-Cu in their respective range of existence. e) Temperature dependence of the overall water occupancy. To calculate the overall water occupancy, the sum of occupancies of the water molecules in the hydrated phase has been multiplied by the percentage of the hydrated phase in the mixture of both phases. f) Thermal analysis (TG trace: blue, DSC trace: red, MS traces for $m/z = 44$ and 18: black). (For interpretation of the references to color in this figure legend, the reader is referred to the Web version of this article.)

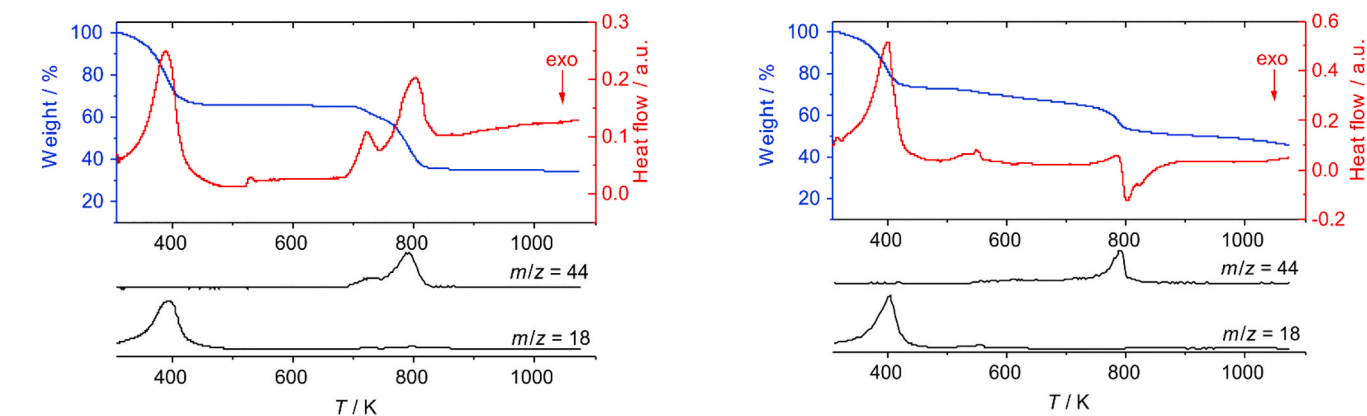


Fig. 6. Thermal analysis of CPO-27-Co (TG trace: blue, DSC trace: red, MS traces for $m/z = 44$ and 18: black). The “wobble” in DSC signal at 523 K is due to a change in heating rate from 2 K min^{-1} to 5 K min^{-1} . (For interpretation of the references to color in this figure legend, the reader is referred to the Web version of this article.)

Fig. 7. Thermal analysis of CPO-27-Zn (TG trace: blue, DSC trace: red, MS traces for $m/z = 44$ and 18: black). The “wobble” in DSC signal at 523 K is due to a change in heating rate from 2 K min^{-1} to 5 K min^{-1} . (For interpretation of the references to color in this figure legend, the reader is referred to the Web version of this article.)

series. For CPO-27-Mg, Co, Mn and Ni the dehydration is a topotactic transition, while discontinuous phase transition are observed for CPO-27-Zn and Cu. The influence of the metal cation on the dehydration is also evident when comparing the onset of decomposition from the VT-PXRD and TG-DSC-MS (see Table 1). Generally, the decomposition of the framework is observed at lower temperatures in the VT-PXRD data than the onset of combustion in the TG-DC-MS data. CPO-27-Co and Zn are an exception, and it was proposed that kinetic effects and the fast heating rate led to an overestimation of the framework stability from the XRD data [58].

A main aspect of interest is to gain a mechanistic understanding of how the water molecules leave the frameworks. Typically, the water molecules located in the center of the pore (O6 and O8) start to leave first, followed by the water molecules in van der Waals contact to the pore surface or hydrogen bonded with the coordinated water (O5 and O7), and finally the coordinated water molecule (O4). This is the case for CPO-27-Co, Mg, Mn and Ni. Also for CPO-27-Zn, O5–O8 leave the framework before O4, even though the situation is more complicated due to the intermediate phase transitions. The coordinated water molecule starts to leave the frameworks at similar temperatures for the CPO-27-M with M = Co (380 K), Ni (365 K), Mg (340 K) and Mn (335 K).

Interestingly, the dehydration process is very different for CPO-27-Cu, where all the water molecules leave at lower temperatures. The coordinated water molecule even starts to leave the framework prior to both O5 and O7, and all the water molecules have left by 335 K. CPO-27-Cu has previously been found to have the weakest interaction and the longest distance between metal cation and coordinated adsorbate molecule, which is a consequence of the Jahn-Teller effect [68,89]. For example, hydrogen sorption studies in the CPO-27-M framework have shown that all the other members of the series have a significantly higher affinity for the adsorbent on the open metal site compared to the other sorption sites. This was found to not be the case for CPO-27-Cu, for which there was no apparent difference in enthalpy of adsorption between the first and second adsorption site. The same behavior is observed during CO₂ adsorption, in that the first and second adsorption sites fill simultaneous in CPO-27-Cu, whereas for the other compounds in the series the first and second adsorption sites are filled predominantly in sequence [68].

The TG-DSC-MS data shows that H₂O evolves immediately for all the members of the series investigated in this study. This is especially evident in the MS trace for H₂O ($m/z = 18$, Fig. 8) and coincides with an endothermic peak in the DSC trace and weight decrease in the TG-traces. In general, this is due to the loss of the non-coordinated water molecules, but for CPO-27-Cu, it also accounts for the loss of the coordinated water molecule.

Despite this common trend, there are noticeable differences between the materials. CPO-27-Cu loses water at a lower temperature than the rest. CPO-27-Co and Mn have similar signal traces, with a maximum just above 400 K. CPO-27-Ni and Mg have maxima around the same temperature, in addition to a significant shoulder around 500 K. CPO-27-Zn has its initial maximum at around 400 K, followed by several smaller peaks at higher temperatures.

For all the members of the series, the initial MS-water signal is typically mirrored in low intensity by the $m/z = 44$ signal, representing evolution of CO₂ (Fig. 9). The origin of this signal at these low

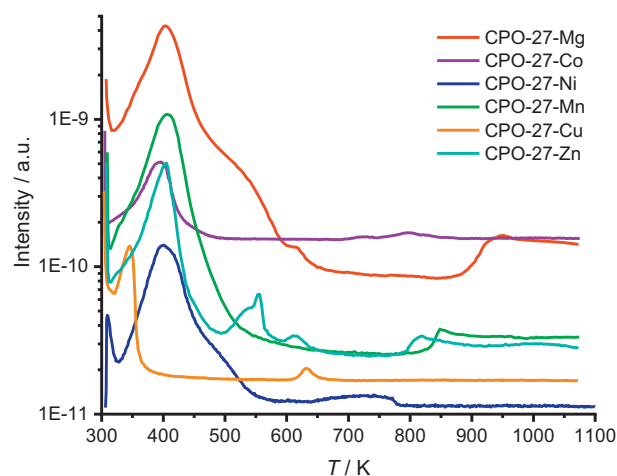


Fig. 8. Comparison of the H₂O evolution in the CPO-27 series as observed by TG-MS.

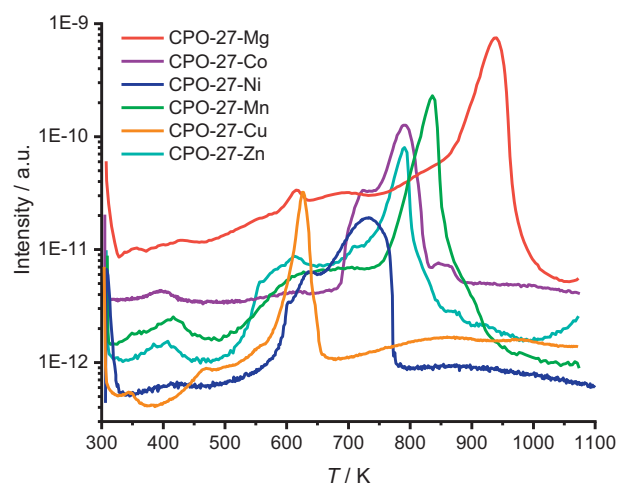


Fig. 9. Comparison of the CO₂ evolution in the CPO-27 series as observed by TG-MS.

temperatures is not entirely clear; we suggest it might indicate decomposition of a small amount of material on the external, more defect prone surface of the crystallites that occurs in parallel with the water evaporation.

All members of the isostructural series do have a relatively stable plateau in the TG trace (Fig. 10), but only CPO-27-Co shows a completely horizontal plateau over a significant temperature range. The other members of the series show a varying degree of a slight decline over the temperature range of the plateau, which is typically mirrored by evolution of water ($m/z = 18$) and/or CO₂ ($m/z = 44$). This tail of the water-signal might be due to residual coordinated water molecules, whilst the evolution of CO₂ is most likely due to a slow, surface-dominated decomposition.

The final decomposition of all the CPO-27 materials is reflected in the respective DSC signal. Notably, for CPO-27-Co the decomposition is shown as two clearly identifiable endothermic peaks, which is mirrored in the MS trace for CO₂ ($m/z = 44$). To a lesser extent this seems to be also the case for CPO-27-Ni (only in MS trace), CPO-27-Mg and CPO-27-Mn. This indicates the presence of at least two overlapping decomposition processes.

Table 1

Comparison of the onset of decomposition observed in VT-PXRD and TG-DSC-MS experiments.

Material	VT-PXRD	TG-DSC-MS
CPO-27-Mg	620/770 K (this work), 510 K [51]	880 K
CPO-27-Ni	540 K [50]	590 K
CPO-27-Mn	515/720 K	770 K
CPO-27-Cu	520 K	570–580 K
CPO-27-Co	723 K [58]	680–690 K
CPO-27-Zn	660 K [58]	500 K (730 K)

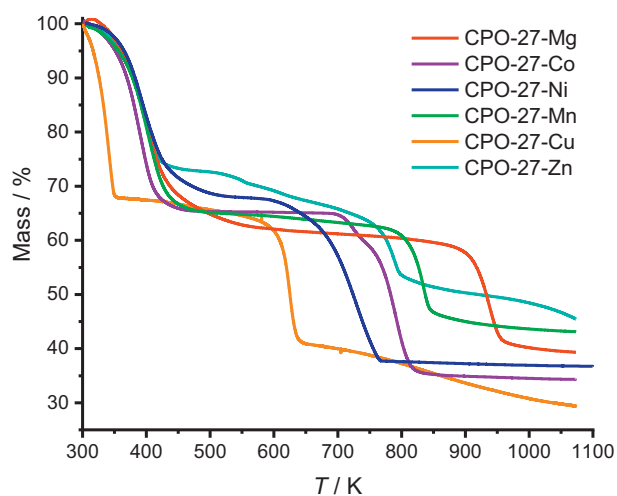


Fig. 10. Comparison of the TG data for the CPO-27-M series.

3.8. Hydration of CPO-27-Co

The structural changes and properties associated with the hydration of CPO-27-Co have also been investigated to confirm the existence of a discontinuous phase transition previously observed on rehydration in a previous experiment [85]. This experimental finding was in contrast to the continuous transition that is observed when transforming from the hydrated to dehydrated structure [58]. However, CPO-27-Co has been shown to undergo phase transitions after adsorption of CO₂ and xylene [91,92]. These differences indicated that it is necessary to gain more insight into the behavior of the material on rehydration. A dehydrated sample was measured by time-resolved PXRD at a temperature of 298 K and under a constant argon stream saturated with water vapor. The diffractograms exhibit good crystallinity of CPO-27-Co during the whole hydration experiment (Fig. 11a). Changes in reflection positions and intensities are observed in the time range of 253–262 min after beginning the experiment (Fig. S21). Specifically, the Rietveld refinements of the powder diffraction data show that from 255 until 261 min two phases coexist (Fig. 11b and Fig. S22). The first phase corresponds to an almost completely dehydrated form of CPO-27-Co (phase I), where only the open metal site is partially coordinated by water (s.o.f. < 0.5). The second phase corresponds to a fully hydrated form of CPO-27-Co (phase II). The changes observed between 253 and 255 min are due to increased hydration of the initial phase I, whilst the changes observed between 261 and 263 min are due to changes in the hydration of phase II.

The conversion between the two phases was also observed visually (see Fig. S23). The hydration front is clearly visible due to the difference in coloration between the dehydrated form (brown-grey, phase I) and the hydrated one (orange-red, phase II), allowing to follow the water adsorption in the upstream part of the capillary. A profile fit at 257 min (Fig. 11c) shows that at this point both phases (hydrated and dehydrated) are present in the pattern, i.e. both phases coexist in the area irradiated by the X-ray beam. Plotting the ratio of the two phases vs. time (min) it is evident that the material transforms from 100% phase I to 100% phase II in less than 10 min (over a range of about 100 scans) (Fig. 11d).

It is intriguing that there appears to be a rapid transition from the empty structure to the fully hydrated one over the beam width. The uptake of water in the structure is *de facto* instantaneous from almost zero to five water molecules per formula unit as the water front passes through. This means that there is a sharp hydration front moving through the bed. This highlights the strength of interaction of CPO-27-Co with water, not only at the open metal site but also for the rest of the adsorption sites.

We can't exactly match the observations here to the ones from the

experiments reported by us previously [85]. Both findings correspond to a co-existence of the hydrated and dehydrated phase. However, in the previous experiment a significant reduction of the PXRD intensities was observed which should indicate the existence of an amorphous intermediary phase during the rehydration process, which was in contrast to the continuous crystallinity during dehydration. This previous finding is clearly not observed in the hydration experiment reported here. It should be mentioned, though, that the CPO-27-Co samples in these two experiments were prepared using different synthesis procedures (e.g. different solvents). This should not affect the dehydration behavior when the desolvated material is structurally identical, unless crystal size effects play an underestimated role. Such size effects have been reported for rigid and flexible MOFs [93–98], but they were beyond the scope of this study to investigate. There are also differences in the experimental setup between the two hydration experiments, such as the continuous flow of saturated water through the sample here. This experiment shows that the rehydration of CPO-27-Co can occur rapidly, in confirmation of thermogravimetric dehydration/hydration experiments [49]. There is no indication of an occurrence of an intermediary non-crystalline phase. It is interesting to point out that the dehydration and rehydration process, as investigated under the conditions described in this study, show profound mechanistic differences. During dehydration (in a dry inert gas stream under heating) a gradual decrease in occupation of the different water sites, distributed over all crystallites in the beam, was observed, while during rehydration (with a very similar experimental setup, but at room temperature with wet gas stream) a given CPO-27-Co crystallite first adsorbs the maximum amount of water possible before breakthrough of water proceeds to the still dehydrated material downstream.

4. Conclusions

We have carried out detailed VT-PXRD and TG-DSC-MS studies of desolvation and rehydration of the CPO-27 family. The results highlight differences and similarities of the members of this series depending on the metal cation.

Whereas VT-PXRD and TG-DSC provide detailed information on the stability of the materials, the evolution of water and CO₂ observed by mass spectrometry gives invaluable information on the dehydration and decomposition processes on a molecular scale. It is interesting to note that the CPO-27 series starts to evolve minute amounts of CO₂ at temperatures slightly above room temperature, long before one expects any decomposition to occur. This experimental finding is ascribed to the decomposition of a small amount of the MOF at the external surface, where it is expected to be more reactive due to the termination of the crystal structure, occurring in parallel with the water evaporation.

The *In situ* VT-PXRD experiment of the rehydration highlights that CPO-27-Co adsorbs water quickly and completely. In an adsorption column, the CPO-27-Co material upstream would adsorb all the water available until it is completely hydrated before CPO-27-Co located downstream starts to adsorb, resulting in a close to maximum achievable capacity (for the material) before breakthrough is observed. No structural degradation is observed by VT-PXRD. The high affinity for water implies that CPO-27-Co could be a suitable candidate for dehumidification applications. We expect the other members of the series, all of which have water uptake capacities larger than 30 wt %, to behave very similarly. For applications such as water harvesting from air or in adsorption chillers one needs materials that are stable upon water exposure, and where the water molecules can be easily released. In this respect, CPO-27-Cu appears to be an especially promising candidate within the CPO-27 series because all the water molecules are released by the comparably low temperature of 360 K.

Actual implementation in water sorption based applications requires significant long term stability of the material and its properties over many adsorption and desorption cycles, and more application oriented studies will be needed to establish the suitability of the CPO-27 materials for heat pump applications [99]. As we have shown here, the different

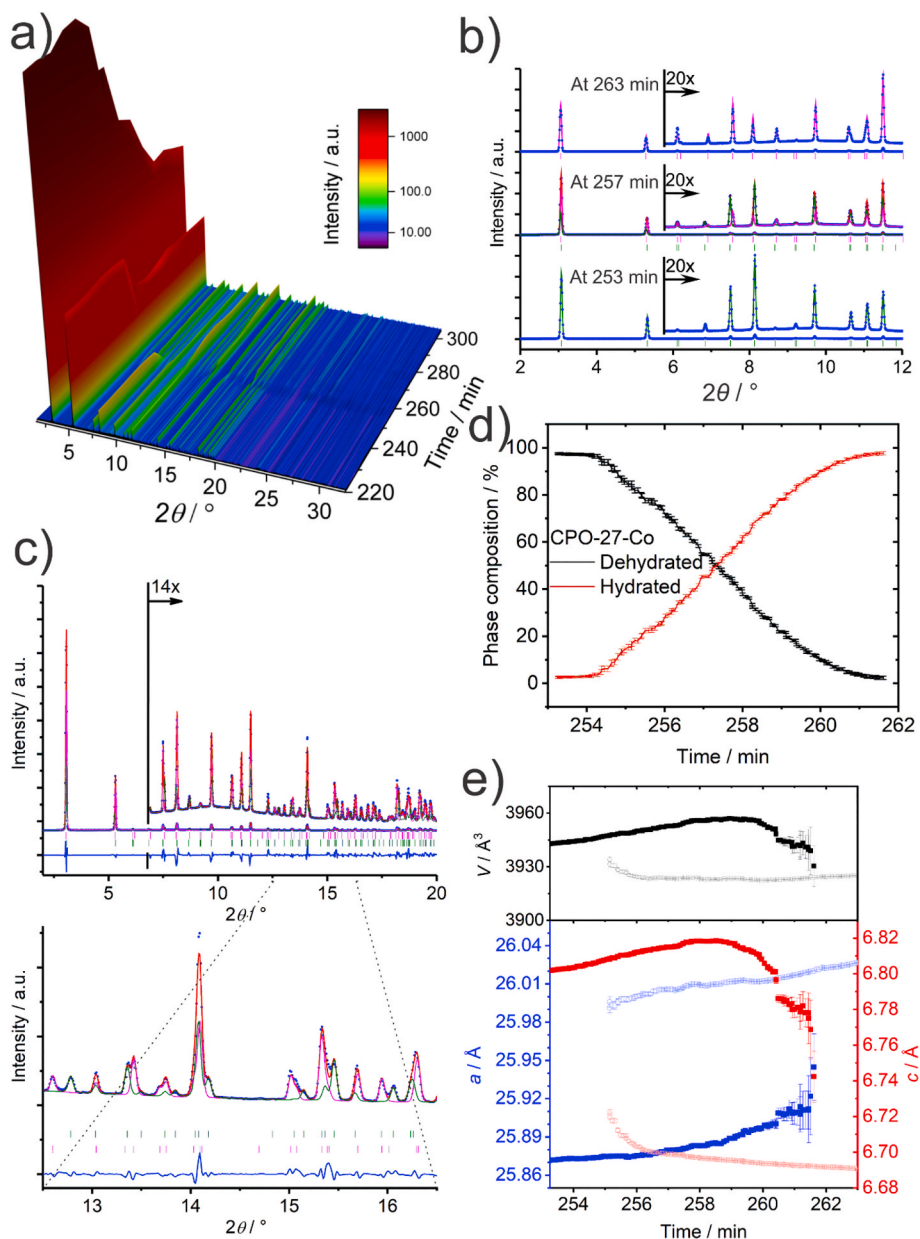


Fig. 11. a) VT-PXRD data of the hydration of originally dehydrated CPO-27-Co in a water saturated Ar stream. b) PXRD patterns, showing the exclusive existence of the dehydrated phase I 253 min after the start of the experiment, a mixture of phase I and II after 257 min, and the exclusive existence of the hydrated phase II after 263 min. The blue points and the red line represent the experimental and calculated diffraction patterns, while the magenta and green lines represent the calculated diffraction patterns. The magenta and green tick marks represent the Bragg reflections for phase II and phase I, respectively. c) Rietveld refinement plot at 257 min, with magnified excerpt of the region from 12.5° to 16.5° . The blue points and the red line represent the experimental and calculated diffraction patterns. The magenta and green lines represent the calculated diffraction patterns for phase II and phase I, respectively. The blue line at the bottom represents the difference between experimental and calculated patterns. The magenta and green tick marks represent the Bragg reflections phase II and phase I, respectively. d) Evolution of the ratio between the two phases. e) The development of unit cell parameters.

CPO-27 materials do behave to varying degrees different in their water sorption properties. Thus, one has to expect that the individual compounds will also behave possibly decisively different in a specific application. Application oriented future studies should therefore also pay attention on identifying which of the materials in the series is most useful for the particular application.

CRediT authorship contribution statement

Mali H. Rosnes: Formal analysis, Investigation, Visualization, Writing - original draft, Writing - review & editing, Funding acquisition. **Breogán Pato-Doldán:** Formal analysis, Visualization, Writing - original draft, Writing - review & editing. **Rune E. Johnsen:** Formal analysis, Investigation, Visualization, Writing - original draft, Writing - review & editing. **Alexander Mundstock:** Investigation, Visualization, Writing - review & editing. **Jürgen Caro:** Conceptualization, Writing - review & editing. **Pascal D.C. Dietzel:** Conceptualization, Methodology, Investigation, Visualization, Writing - review & editing, Supervision, Project administration, Funding acquisition.

Declaration of competing interest

The authors declare that they have no known competing financial interests or personal relationships that could have appeared to influence the work reported in this paper.

Acknowledgement

The authors would like to thank Dr. Dmitry Chernyshov, Dr. Alexey Mikheykin, Dr. Vadim Diadkin, and Dr. Wouter van Beek at the Swiss-Norwegian Beamlines for their support in performing the experiments at the ESRF, and acknowledge the support from the Research Council of Norway through the FRINATEK Program (grant 221596), ISP-KJEMI Program (grant 209339) and SYNKNOYT (grants 227702 and 247734).

Appendix A. Supplementary data

Supplementary data to this article can be found online at <https://doi.org/10.1016/j.micromeso.2020.110503>.

References

- [1] S.R. Batten, N.R. Champness, X.M. Chen, J. Garcia-Martinez, S. Kitagawa, L. Ohrstrom, M. O'Keeffe, M.P. Suh, J. Reedijk, Terminology of metal-organic frameworks and coordination polymers (IUPAC Recommendations 2013), *Pure Appl. Chem.* 85 (2013) 1715–1724.
- [2] Q. Wang, D. Astruc, State of the art and prospects in metal-organic framework (MOF)-based and MOF-derived nanocatalysis, *Chem. Rev.* 120 (2020) 1438–1511.
- [3] L. Jiao, H.-L. Jiang, Metal-organic-framework-based single-atom catalysts for energy applications, *Chem.* 5 (2019) 786–804.
- [4] S.M.J. Rogge, A. Bavykina, J. Hajek, H. Garcia, A.I. Olivos-Suarez, A. Sepulveda-Escribano, A. Vimont, G. Clet, P. Bazin, F. Kapteijn, M. Daturi, E.V. Ramos-Fernandez, F.X. Llabres i Xamena, V. Van Speybroeck, J. Gascon, Metal-organic and covalent organic frameworks as single-site catalysts, *Chem. Soc. Rev.* 46 (2017) 3134–3184.
- [5] R.-B. Lin, S. Xiang, H. Xing, W. Zhou, B. Chen, Exploration of porous metal-organic frameworks for gas separation and purification, *Coord. Chem. Rev.* 378 (2019) 87–103.
- [6] M. Ding, R.W. Flaig, H.-L. Jiang, O.M. Yaghi, Carbon capture and conversion using metal-organic frameworks and MOF-based materials, *Chem. Soc. Rev.* 48 (2019) 2783–2828.
- [7] H. Li, K. Wang, Y. Sun, C.T. Lollar, J. Li, H.-C. Zhou, Recent advances in gas storage and separation using metal-organic frameworks, *Mater. Today* 21 (2018) 108–121.
- [8] B.R. Barnett, M.I. Gonzalez, J.R. Long, Recent progress towards light hydrocarbon separations using Metal-Organic frameworks, *Trends Chem* 1 (2019) 159–171.
- [9] X. Zhao, Y. Wang, D.-S. Li, X. Bu, P. Feng, Metal-organic frameworks for separation, *Adv. Mater.* 30 (2018) 1705189.
- [10] C.H. Hendon, A.J. Rieth, M.D. Korzyński, M. Dincă, Grand challenges and future opportunities for metal-organic frameworks, *ACS Cent. Sci.* 3 (2017) 554–563.
- [11] I. Stassen, N. Burch, A. Talin, P. Falcaro, M. Allendorf, R. Ameloot, An updated roadmap for the integration of metal-organic frameworks with electronic devices and chemical sensors, *Chem. Soc. Rev.* 46 (2017) 3185–3241.
- [12] W.P. Lustig, S. Mukherjee, N.D. Rudd, A.V. Desai, J. Li, S.K. Ghosh, Metal-organic frameworks: functional luminescent and photonic materials for sensing applications, *Chem. Soc. Rev.* 46 (2017) 3242–3285.
- [13] F.-Y. Yi, D. Chen, M.-K. Wu, L. Han, H.-L. Jiang, Chemical sensors based on metal-organic frameworks, *ChemPlusChem* 81 (2016) 675–690.
- [14] K. Uemura, R. Matsuda, S. Kitagawa, Flexible microporous coordination polymers, *J. Solid State Chem.* 178 (2005) 2420–2429.
- [15] S. Kitagawa, K. Uemura, Dynamic porous properties of coordination polymers inspired by hydrogen bonds, *Chem. Soc. Rev.* 34 (2005) 109–119.
- [16] N.C. Burch, H. Jasuja, K.S. Walton, Water stability and adsorption in metal-organic frameworks, *Chem. Rev.* 114 (2014) 10575–10612.
- [17] A.J. Howarth, A.W. Peters, N.A. Vermeulen, T.C. Wang, J.T. Hupp, O.K. Farha, Best practices for the synthesis, activation, and characterization of metal-organic frameworks, *Chem. Mater.* 29 (2017) 26–39.
- [18] S.K. Henninger, F. Jeremias, H. Kummer, C. Janiak, MOFs for use in adsorption heat pump processes, *Eur. J. Inorg. Chem.* 2012 (2012) 2625–2634.
- [19] F. Jeremias, D. Fröhlich, C. Janiak, S.K. Henninger, Water and methanol adsorption on MOFs for cycling heat transformation processes, *New J. Chem.* 38 (2014) 1846–1852.
- [20] M.F. de Lange, K.J.F.M. Verouden, T.J.H. Vlucht, J. Gascon, F. Kapteijn, Adsorption-Driven heat pumps: the potential of metal-organic frameworks, *Chem. Rev.* 115 (2015) 12205–12250.
- [21] H. Kummer, F. Jeremias, A. Warlo, G. Földner, D. Fröhlich, C. Janiak, R. Gläser, S. K. Henninger, A functional full-scale heat exchanger coated with aluminum fumarate metal-organic framework for adsorption heat transformation, *Ind. Eng. Chem. Res.* 56 (2017) 8393–8398.
- [22] J. Zheng, R.S. Vemuri, L. Estevez, P.K. Koech, T. Varga, D.M. Camaioni, T.A. Blake, B.P. McGrail, R.K. Motkuri, Pore-engineered metal-organic frameworks with excellent adsorption of water and fluorocarbon refrigerant for cooling applications, *J. Am. Chem. Soc.* 139 (2017) 10601–10604.
- [23] L. Garzón-Tovar, J. Pérez-Carvajal, I. Imaz, D. Maspoch, Composite salt in porous metal-organic frameworks for adsorption heat transformation, *Adv. Funct. Mater.* 27 (2017) 1606424.
- [24] S. Cui, M. Qin, A. Marandi, V. Steggle, S. Wang, X. Feng, F. Nouar, C. Serre, Metal-Organic Frameworks as advanced moisture sorbents for energy-efficient high temperature cooling, *Sci. Rep.* 8 (2018) 15284.
- [25] J.S. Lee, J.W. Yoon, P.G.M. Mileo, K.H. Cho, J. Park, K. Kim, H. Kim, M.F. de Lange, F. Kapteijn, G. Maurin, S.M. Humphrey, J.-S. Chang, Porous metal-organic framework CUK-1 for adsorption heat allocation toward green applications of natural refrigerant water, *ACS Appl. Mater. Interfaces* 11 (2019) 25778–25789.
- [26] M. Wöllner, N. Klein, S. Kaskel, Measuring water adsorption processes of metal-organic frameworks for heat pump applications via optical calorimetry, *Microporous Mesoporous Mater.* 278 (2019) 206–211.
- [27] S. Göpkinsar, S.-J. Ernst, E. Hastürk, M. Möllers, I. El Aita, R. Wiedey, N. Tannert, S. Nießing, S. Abdpour, A. Schmitz, J. Quodbach, G. Földner, S.K. Henninger, C. Janiak, Air-con metal-organic frameworks in binder composites for water adsorption heat transformation systems, *Ind. Eng. Chem. Res.* 58 (2019) 21493–21503.
- [28] N. Hanikel, M.S. Prévot, O.M. Yaghi, MOF water harvesters, *Nat. Nanotechnol.* 15 (2020) 348–355.
- [29] A. Karmakar, V. Prabakaran, D. Zhao, K.J. Chua, A review of metal-organic frameworks (MOFs) as energy-efficient desiccants for adsorption driven heat-transformation applications, *Appl. Energy* 269 (2020) 115070.
- [30] J. Canivet, A. Fateeva, Y. Guo, B. Coasne, D. Farrusseng, Water adsorption in MOFs: fundamentals and applications, *Chem. Soc. Rev.* 43 (2014) 5594–5617.
- [31] C. Serre, F. Millange, C. Thouvenot, M. Noguès, G. Marsolier, D. Louër, G. Férey, Very large breathing effect in the first nanoporous chromium(III)-Based solids: MIL-53 or Cr^{III}(OH)-(O₂C-C₆H₄-CO₂)-(HO₂C-C₆H₄-CO₂H)_x·H₂O_y, *J. Am. Chem. Soc.* 124 (2002) 13519–13526.
- [32] F. Millange, C. Serre, G. Férey, Synthesis, structure determination and properties of MIL-53as and MIL-53ht: the first Cr^{III} hybrid inorganic-organic microporous solids: Cr^{III}(OH)-(O₂C-C₆H₄-CO₂)-(HO₂C-C₆H₄-CO₂H)_x, *Chem. Commun.* (2002) 822–823.
- [33] T. Loiseau, C. Serre, C. Huguenard, G. Fink, F. Taulelle, M. Henry, T. Bataille, G. Férey, A rationale for the large breathing of the porous aluminum terephthalate (MIL-53) upon hydration, *Chem. Eur. J.* 10 (2004) 1373–1382.
- [34] C. Serre, C. Mellot-Draznics, S. Surlé, N. Audebrand, Y. Filinchuk, G. Férey, Role of solvent-host interactions that lead to very large swelling of hybrid frameworks, *Science* 315 (2007) 1828–1831.
- [35] H. Reinsch, R.S. Pillai, R. Siegel, J. Senker, A. Lieb, G. Maurin, N. Stock, Structure and properties of Al-MIL-53-ADP, a breathing MOF based on the aliphatic linker molecule adipic acid, *Dalton Trans.* 45 (2016) 4179–4186.
- [36] A.D.G. Firmino, R.F. Mendes, M.M. Antunes, P.C. Barbosa, S.M.F. Vilela, A. A. Valente, F.M.L. Figueiredo, J.P.C. Tomé, F.A.A. Paz, Robust multifunctional yttrium-based metal-organic frameworks with breathing effect, *Inorg. Chem.* 56 (2017) 1193–1208.
- [37] K. Biradha, M. Fujita, A springlike 3D-coordination network that shrinks or swells in a crystal-to-crystal manner upon guest removal or re-adsorption, *Angew. Chem. Int. Ed.* 41 (2002) 3392–3395.
- [38] T.K. Maji, G. Mostafa, R. Matsuda, S. Kitagawa, Guest-Induced asymmetry in a Metal-Organic porous solid with reversible single-crystal-to-single-crystal structural transformation, *J. Am. Chem. Soc.* 127 (2005) 17152–17153.
- [39] J.-P. Zhang, Y.-Y. Lin, W.-X. Zhang, X.-M. Chen, Temperature- or guest-induced drastic single-crystal-to-single-crystal transformations of a nanoporous coordination polymer, *J. Am. Chem. Soc.* 127 (2005) 14162–14163.
- [40] G.J. Halder, C.J. Kepert, In situ single-crystal X-ray diffraction studies of desorption and sorption in a flexible nanoporous molecular framework material, *J. Am. Chem. Soc.* 127 (2005) 7891–7900.
- [41] P.K. Allan, B. Xiao, S.J. Teat, J.W. Knight, R.E. Morris, In situ single-crystal diffraction studies of the structural transition of Metal-Organic framework copper 5-sulfoisophthalate, Cu-SIP-3, *J. Am. Chem. Soc.* 132 (2010) 3605–3611.
- [42] D. Sarma, S. Natarajan, Usefulness of in situ single crystal to single crystal transformation (SCSC) studies in understanding the temperature-dependent dimensionality cross-over and structural reorganization in copper-containing metal-organic frameworks (MOFs), *Cryst. Growth Des.* 11 (2011) 5415–5423.
- [43] M.P. Suh, Y.E. Cheon, E.Y. Lee, Reversible transformation of Zn^{II} coordination geometry in a single crystal of porous metal-organic framework [Zn₃(ntb)₂(EtOH)₂]-4 EtOH, *Chem. Eur. J.* 13 (2007) 4208–4215.
- [44] C.-L. Chen, A.M. Goforth, M.D. Smith, C.-Y. Su, H.-C. Zur Loye, [Co₂(ppca)₂(H₂O)(V₄O₁₂)_{0.5}]: a framework material exhibiting reversible shrinkage and expansion through a single-crystal-to-single-crystal transformation involving a change in the cobalt coordination environment, *Angew. Chem. Int. Ed.* 44 (2005) 6673–6677.
- [45] J. Jia, X. Lin, A.J. Blake, N.R. Champness, P. Hubberstey, L. Shao, G. Walker, C. Wilson, M. Schröder, Triggered ligand release coupled to framework Rearrangement: generating crystalline porous coordination materials, *Inorg. Chem.* 45 (2006) 8838–8840.
- [46] A.A. Bezrukov, K.W. Törnroos, P.D.C. Dietzel, Variation of desolvation behavior in two isostructural metal-organic frameworks based on a flexible, racemic bifunctional organic linker, *Eur. J. Inorg. Chem.* 2016 (2016) 4430–4439.
- [47] D. Bradshaw, J.E. Warren, M.J. Rosseinsky, Reversible concerted ligand substitution at alternating metal sites in an extended solid, *Science* 315 (2007) 977–980.
- [48] T. Tahier, C.L. Oliver, In situ variable-temperature single crystal X-ray diffraction studies of the single-crystal-to-single-crystal dehydration and rehydration of a mixed-ligand 2D zinc metal-organic framework using trimesate and 4,4'-bipyridine-N,N'-dioxide as ligands, *CrystEngComm* 17 (2015) 8946–8956.
- [49] P.D.C. Dietzel, Y. Morita, R. Blom, H. Fjellvåg, An in situ high-temperature single-crystal investigation of a dehydrated metal-organic framework compound and field-induced magnetization of one-dimensional metal-oxygen chains, *Angew. Chem. Int. Ed.* 44 (2005) 6354–6358.
- [50] P.D.C. Dietzel, B. Panella, M. Hirscher, R. Blom, H. Fjellvåg, Hydrogen adsorption in a nickel based coordination polymer with open metal sites in the cylindrical cavities of the desolvated framework, *Chem. Commun.* (2006) 959–961.
- [51] P.D.C. Dietzel, R. Blom, H. Fjellvåg, Base-Induced formation of two magnesium metal-organic framework compounds with a bifunctional tetratopic ligand, *Eur. J. Inorg. Chem.* (2008) 3624–3632.
- [52] W. Zhou, H. Wu, T. Yildirim, Enhanced H₂ adsorption in isostructural metal-organic frameworks with open metal sites: strong dependence of the binding strength on metal ions, *J. Am. Chem. Soc.* 130 (2008) 15268–15269.
- [53] N.L. Rosi, J. Kim, M. Eddaoudi, B. Chen, M. O'Keeffe, O.M. Yaghi, Rod packings and Metal-Organic frameworks constructed from rod-shaped secondary building units, *J. Am. Chem. Soc.* 127 (2005) 1504–1518.

- [54] M. Márcz, R.E. Johnsen, P.D.C. Dietzel, H. Fjellvåg, The iron member of the CPO-27 coordination polymer series: synthesis, characterization, and intriguing redox properties, *Microporous Mesoporous Mater.* 157 (2012) 62–74.
- [55] E.D. Bloch, L.J. Murray, W.L. Queen, S. Chavan, S.N. Maximoff, J.P. Bigi, R. Krishna, V.K. Peterson, F. Grandjean, G.J. Long, B. Smit, S. Bordiga, C.M. Brown, J.R. Long, Selective binding of O₂ over N₂ in a redox-active metal-organic framework with open iron(II) coordination sites, *J. Am. Chem. Soc.* 133 (2011) 14814–14822.
- [56] R. Sanz, F. Martinez, G. Orcajo, L. Wojtas, D. Briones, Synthesis of a honeycomb-like Cu-based metal-organic framework and its carbon dioxide adsorption behaviour, *Dalton Trans.* 42 (2013) 2392–2398.
- [57] F. Bonino, S. Chavan, J.G. Vitillo, E. Groppo, G. Agostini, C. Lamberti, P.D. Dietzel, C. Prestipino, S. Bordiga, Local structure of CPO-27-Ni metalloorganic framework upon dehydration and coordination of NO, *Chem. Mater.* 20 (2008) 4957–4968.
- [58] P.D.C. Dietzel, R.E. Johnsen, R. Blom, H. Fjellvåg, Structural changes and coordinatively unsaturated metal atoms on dehydration of honeycomb analogous microporous metal-organic frameworks, *Chem. Eur. J.* 14 (2008) 2389–2397.
- [59] Y. Liu, H. Kabbour, C.M. Brown, D.A. Neumann, C.C. Ahn, Increasing the density of adsorbed hydrogen with coordinatively unsaturated metal centers in metal-organic frameworks, *Langmuir* 24 (2008) 4772–4777.
- [60] J.G. Vitillo, L. Regli, S. Chavan, G. Ricchiardi, G. Spoto, P.D.C. Dietzel, S. Bordiga, A. Zecchina, Role of exposed metal sites in hydrogen storage in MOFs, *J. Am. Chem. Soc.* 130 (2008) 8386–8396.
- [61] A.C. McKinlay, B. Xiao, D.S. Wragg, P.S. Wheatley, I.L. Megson, R.E. Morris, Exceptional behavior over the whole adsorption-storage-delivery cycle for NO in porous metal organic frameworks, *J. Am. Chem. Soc.* 130 (2008) 10440–10444.
- [62] P.D.C. Dietzel, R.E. Johnsen, H. Fjellvåg, S. Bordiga, E. Groppo, S. Chavan, R. Blom, Adsorption properties and structure of CO₂ adsorbed on open coordination sites of metal-organic framework Ni₂(dhtp) from gas adsorption, IR spectroscopy and X-ray diffraction, *Chem. Commun.* (2008) 5125–5127.
- [63] P.D.C. Dietzel, V. Besikiotis, R. Blom, Application of metal-organic frameworks with coordinatively unsaturated metal sites in storage and separation of methane and carbon dioxide, *J. Mater. Chem.* 19 (2009) 7362–7370.
- [64] S. Xiang, W. Zhou, Z. Zhang, M.A. Green, Y. Liu, B. Chen, Open metal sites within isostructural metal-organic frameworks for differential recognition of acetylene and extraordinarily high acetylene storage capacity at room temperature, *Angew. Chem. Int. Ed.* 49 (2010) 4615–4618.
- [65] P.D.C. Dietzel, P.A. Georgiev, J. Eckert, R. Blom, T. Strässle, T. Unruh, Interaction of hydrogen with accessible metal sites in the metal-organic frameworks M₂(dhtp) (CPO-27-M; M = Ni, Co, Mg), *Chem. Commun.* 46 (2010) 4962–4964.
- [66] D. Yu, A.O. Yazaydin, J.R. Lane, P.D.C. Dietzel, R.Q. Snurr, A combined experimental and quantum chemical study of CO₂ adsorption in the metal-organic framework CPO-27 with different metals, *Chem. Sci.* 4 (2013) 3544–3556.
- [67] J.S. Lee, B. Vlasisavljevich, D.K. Britt, C.M. Brown, M. Haranczyk, J.B. Neaton, B. Smit, J.R. Long, W.L. Queen, Understanding small-molecule interactions in metal-organic frameworks: coupling experiment with theory, *Adv. Mater.* 27 (2015) 5785–5796.
- [68] B. Pato-Doldán, M.H. Rosnes, P.D.C. Dietzel, An in-depth structural study of the carbon dioxide adsorption process in the porous metal-organic frameworks CPO-27-M, *ChemSusChem* 10 (2017) 1710–1719.
- [69] I. Strauss, A. Mundstock, D. Hinrichs, R. Himstedt, A. Knebel, C. Reinhardt, D. Dorfs, J. Caro, The interaction of guest molecules with Co-MOF-74: a vis/NIR and Raman approach, *Angew. Chem. Int. Ed.* 57 (2018) 7434–7439.
- [70] Ü. Kökçam-Demir, A. Goldman, L. Esrafilı, M. Gharib, A. Morsali, O. Weingart, C. Janiak, Coordinatively unsaturated metal sites (open metal sites) in metal-organic frameworks: design and applications, *Chem. Soc. Rev.* 49 (2020) 2751–2798.
- [71] H. Furukawa, F. Gándara, Y.-B. Zhang, J. Jiang, W.L. Queen, M.R. Hudson, O. M. Yaghi, Water adsorption in porous metal-organic frameworks and related materials, *J. Am. Chem. Soc.* 136 (2014) 4369–4381.
- [72] P. Guo, A.G. Wong-Foy, A.J. Matzger, Microporous coordination polymers as efficient sorbents for air dehumidification, *Langmuir* 30 (2014) 1921–1925.
- [73] X. Peng, L.-C. Lin, W. Sun, B. Smit, Water adsorption in metal-organic frameworks with open-metal sites, *AlChE J.* 61 (2015) 677–687.
- [74] K. Tan, S. Zuluaga, Q. Gong, P. Canepa, H. Wang, J. Li, Y.J. Chabal, T. Thonhauser, Water reaction mechanism in metal organic frameworks with coordinatively unsaturated metal ions: MOF-74, *Chem. Mater.* 26 (2014) 6886–6895.
- [75] J. Liu, A.I. Benin, A.M.B. Furtado, P. Jakubczak, R.R. Willis, M.D. LeVan, Stability effects on CO₂ adsorption for the DOBDC series of metal-organic frameworks, *Langmuir* 27 (2011) 11451–11456.
- [76] J.B. DeCoste, G.W. Peterson, B.J. Schindler, K.L. Killops, M.A. Browe, J.J. Mahle, The effect of water adsorption on the structure of the carboxylate containing metal-organic frameworks Cu-BTC, Mg-MOF-74, and UiO-66, *J. Mater. Chem.* 1 (2013) 11922–11932.
- [77] T. Remy, S.A. Peter, S. Van der Perre, P. Valvekens, D.E. De Vos, G.V. Baron, J.F. M. Denayer, Selective dynamic CO₂ separations on Mg-MOF-74 at low pressures: a detailed comparison with 13X, *J. Phys. Chem. C* 117 (2013) 9301–9310.
- [78] P.M. Schoenecker, C.G. Carson, H. Jasuja, C.J.J. Flemming, K.S. Walton, Effect of water adsorption on retention of structure and surface area of metal-organic frameworks, *Ind. Eng. Chem. Res.* 51 (2012) 6513–6519.
- [79] A.C. Kizzie, A.G. Wong-Foy, A.J. Matzger, Effect of humidity on the performance of microporous coordination polymers as adsorbents for CO₂ capture, *Langmuir* 27 (2011) 6368–6373.
- [80] K. Tan, N. Nijem, Y. Gao, S. Zuluaga, J. Li, T. Thonhauser, Y.J. Chabal, Water interactions in metal organic frameworks, *CrystEngComm* 17 (2015) 247–260.
- [81] S. Zuluaga, E.M.A. Fuentes-Fernandez, K. Tan, F. Xu, J. Li, Y.J. Chabal, T. Thonhauser, Understanding and controlling water stability of MOF-74, *J. Mater. Chem.* 4 (2016) 5176–5183.
- [82] N. Drenchev, M. Mihaylov, P.D.C. Dietzel, A. Albinati, P.A. Georgiev, K. Hadjiivanov, Low-temperature adsorption of H₂ and D₂ on dehydrated and water precovered CPO-27-Ni, *J. Phys. Chem. C* 120 (2016) 23083–23092.
- [83] Y. Jiao, C.R. Morelock, N.C. Burtch, W.P. Mounfield, J.T. Hungerford, K.S. Walton, Tuning the kinetic water stability and adsorption interactions of Mg-MOF-74 by partial substitution with Co or Ni, *Ind. Eng. Chem. Res.* 54 (2015) 12408–12414.
- [84] Y. Li, X. Wang, D. Xu, J.D. Chung, M. Kaviani, B. Huang, H₂O adsorption/desorption in MOF-74: Ab initio molecular dynamics and experiments, *J. Phys. Chem. C* 119 (2015) 13021–13031.
- [85] C. Chmelik, A. Mundstock, P.D.C. Dietzel, J. Caro, Idiosyncrasies of Co₂(dhtp) in situ-annealing by methanol, *Microporous Mesoporous Mater.* 183 (2014) 117–123.
- [86] P. Norby, Hydrothermal conversion of zeolites: an in situ synchrotron X-ray powder diffraction study, *J. Am. Chem. Soc.* 119 (1997) 5215–5221.
- [87] A.A. Coelho, J. Evans, I. Evans, A. Kern, S. Parsons, The TOPAS symbolic computation system, *Powder Diffr.* 26 (2012) S22–S25.
- [88] J.S.O. Evans, Advanced input files & parametric quantitative analysis using topas, *Mater. Sci. Forum* 651 (2010) 1–9.
- [89] M.H. Rosnes, M. Opitz, M. Frontzek, W. Lohstroh, J.P. Embs, P.A. Georgiev, P.D. C. Dietzel, Intriguing differences in hydrogen adsorption in CPO-27 materials induced by metal substitution, *J. Mater. Chem.* 3 (2015) 4827–4839.
- [90] M.H. Rosnes, F.S. Nesse, M. Opitz, P.D.C. Dietzel, Morphology control in modulated synthesis of metal-organic framework CPO-27, *Microporous Mesoporous Mater.* 275 (2019) 207–213.
- [91] M.I. Gonzalez, M.T. Kapelewski, E.D. Bloch, P.J. Milner, D.A. Reed, M.R. Hudson, J.A. Mason, G. Barin, C.M. Brown, J.R. Long, Separation of xylene isomers through multiple metal site interactions in metal-organic frameworks, *J. Am. Chem. Soc.* 140 (2018) 3412–3422.
- [92] B. Pato-Doldán, M.H. Rosnes, D. Chernyshov, P.D.C. Dietzel, Carbon dioxide induced structural phase transition in metal-organic frameworks CPO-27, *CrystEngComm* 22 (2020) 4353–4358.
- [93] Y. Hijikata, S. Horike, D. Tanaka, J. Groll, M. Mizuno, J. Kim, M. Takata, S. Kitagawa, Differences of crystal structure and dynamics between a soft porous nanocrystal and a bulk crystal, *Chem. Commun.* 47 (2011) 7632–7634.
- [94] C. Zhang, J.A. Gee, D.S. Sholl, R.P. Lively, Crystal-size-dependent structural transitions in nanoporous crystals: adsorption-induced transitions in ZIF-8, *J. Phys. Chem. C* 118 (2014) 20727–20733.
- [95] O.M. Linder-Patton, W.M. Bloch, C.J. Coghlan, K. Sumida, S. Kitagawa, S. Furukawa, C.J. Doonan, C.J. Sumbly, Particle size effects in the kinetic trapping of a structurally-locked form of a flexible MOF, *CrystEngComm* 18 (2016) 4172–4179.
- [96] S. Krause, V. Bon, I. Senkovska, D.M. Többsen, D. Wallacher, R.S. Pillai, G. Maurin, S. Kaskel, The effect of crystallite size on pressure amplification in switchable porous solids, *Nat. Commun.* 9 (2018) 1573.
- [97] O.M. Linder-Patton, B.T. Rogers, K. Sumida, Impact of higher-order structuralization on the adsorption properties of metal-organic frameworks, *Chem. Asian J.* 13 (2018) 1979–1991.
- [98] T. Kundu, M. Wahiduzzaman, B.B. Shah, G. Maurin, D. Zhao, Solvent-Induced control over breathing behavior in flexible metal-organic frameworks for natural-gas delivery, *Angew. Chem. Int. Ed.* 58 (2019) 8073–8077.
- [99] B. Shi, R. Al-Dadah, S. Mahmoud, A. Elsayed, E. Elsayed, CPO-27(Ni) metal-organic framework based adsorption system for automotive air conditioning, *Appl. Therm. Eng.* 106 (2016) 325–333.